The Astrophysical Journal, 954:34 (12pp), 2023 September 1 https://doi.org/10.3847/1538-4357/ace692

The Cygnus Loop: Shock Precursors and Electron–Ion Equilibration

John C. Raymond[1], Ji Yeon Seok[2,3,11], Bon-Chul Koo[4], Igor V. Chilingarian[5,6], Kirill Grishin[7,8], Nelson Caldwell[1], Min Xie[9], and Robert Fesen[10]
[1] Harvard-Smithsonian Center for Astrophysics, 60 Garden St., Cambridge, MA 02138, USA; jraymond@cfa.harvard.edu
[2] Key Laboratory of Optical Astronomy, National Astronomical Observatories, Chinese Academy of Sciences, Beijing 100010, People's Republic of China
[3] Korea Astronomy and Space Science Institute, Daejeon, 305-348, Republic of Korea
[4] Department of Physics and Astronomy, Seoul National University, 1 Gwanak-ro, Gwanak-gu, Seoul 08826, Republic of Korea
[5] Center for Astrophysics—Harvard & Smithsonian, 60 Garden St., Cambridge, MA 02138, USA
[6] Sternberg Astronomical Institute, M.V.Lomonosov Moscow State University, Universitetsky prospect 13, Moscow, 119234, Russia
[7] APC, AstroParticule et Cosmologie, Université Paris Diderot, CNRS/IN2P3, CEA/lrfu, Observatoire de Paris, Sorbonne Paris Cité, 10 rue Alice Domon et Léonie Duquet, 75205, Paris Cedex 13, France
[8] Sternberg Astronomical Institute, Moscow M.V. Lomonosov State University, Universitetskij pr., 13, Moscow 119234, Russia
[9] 136 Bricknell Lane, Coppell, TX 75019, USA
[10] 6127 Wilder Lab, Department of Physics and Astronomy, Dartmouth College, Hanover, NH 03755, USA
Received 2023 June 12; revised 2023 July 10; accepted 2023 July 10; published 2023 August 22

Abstract

The outermost edges of some supernova remnants are marked by filaments of pure Balmer line emission produced by nonradiative shock fronts. The Hα profiles of these filaments provide the shock speed and electron–proton temperature ratio in the shock. We have used the Hectochelle multiobject spectrograph on the MMT telescope to observe nine positions along the eastern nonradiative filaments of the Cygnus Loop, thereby extending the studies of Medina et al. to lower shock speeds. We complement the spectra with images from 1993 to 2020 to measure proper motions to further constrain the parameters. We also present observations of the photoionization precursor to show that the gas is strongly heated, and that the Hα emission from the precursor is dominated by collisional excitation rather than recombination.

Unified Astronomy Thesaurus concepts: Supernova remnants (1667); Interstellar plasma (851)

1. Introduction

The bright optical emission from supernova remnants (SNRs) originates in *radiative* shock waves, which cool from the postshock temperature to ~1000 K or less, converting nearly all the thermal energy of the shocked gas into radiation. On the other hand, *nonradiative* shocks are faster shocks in low-density gas, and their radiative cooling times are longer than the age of the SNR or some other relevant timescale. The nonradiative shocks produce the X-ray emission of SNRs, and they probably dominate the production of cosmic rays. SNR shocks are generally collisionless, which not only means that they can produce cosmic rays but also that different particle species can have different temperatures. For example, if each particle species independently randomizes most the speed of the shock, with no exchange of energy among species, then the thermal energy of each particle will be proportional to its mass.

A nonradiative shock in partially neutral gas will produce Hα emission, since some of the neutral hydrogen atoms passing through the shock will be excited before they are ionized. Since the neutrals do not feel the electromagnetic fields or the turbulence of the collisionless shock, some of them will be excited by electrons and produce a line profile corresponding to the preshock velocity distribution. The line width will include their thermal width and any turbulence, and it may reflect conditions in a photoionization precursor or a thin precursor produced by cosmic rays or a flux of postshock neutrals that overtake the shock (Hester et al. 1994; Morlino et al. 2012; Medina et al. 2014).

However, some of the neutrals will undergo a charge-transfer interaction with a postshock proton, producing a population of neutrals with approximately the postshock proton velocity distribution (Chevalier & Raymond 1978; Bychkov & Lebedev 1979). Excitation of those neutrals will produce a broad component in the Hα profile, whose FWHM is comparable to the shock speed. The intensity ratio of the narrow and broad components depends on the ratio of the ionization rate to the charge-transfer rate, so it is sensitive to the electron temperature, while the velocity width of the broad component is a fairly direct measure of the proton temperature (Laming et al. 1996; Ghavamian et al. 2001; Heng 2010). While relatively slow SNR shocks show nearly complete electron–ion and ion–ion equilibration, fast SNR shocks show very little equilibration (Korreck et al. 2004; Ghavamian et al. 2013; Raymond et al. 2015, 2017). The electron–ion equilibration is especially important because the electron temperature is vital for diagnostics and acceleration of electrons. While the SNR results are somewhat analogous to measurements in the solar wind and to predictions from numerical simulations, they are in violent disagreement for the relatively low shock speeds studied here (Raymond et al. 2023).

The Cygnus Loop is the prototypical middle-aged SNR. It is nearby, at 725 ± 15 pc (Fesen et al. 2021), and it is only lightly reddened, so it has been studied in detail. It is about 18 pc in radius and about 21,000 yr old (Fesen et al. 2018). On its east and west limbs it encounters relatively dense clouds, giving rise to bright radiative shock waves of about 150 km s^{-1}, while

[11] LAMOST Fellow.

toward the north and south the shocks encounter lower densities. There, the gas behind the 350–450 km s^{-1} shocks has not had time to cool, and these nonradiative shocks produce X-ray emission. Some authors have treated the Cygnus Loop as an explosion in a cavity produced by the progenitor star (Leahy 2003; Zhou et al. 2010; Meyer et al. 2015; Fang et al. 2017), but Fesen et al. (2018) find that a Sedov solution matches the temperature, density, and radius of the nonradiative portions quite well.

Pure Balmer line filaments outline the X-ray emission around the northern half of the Cygnus Loop, and very faint Balmer line emission is seen in the south as well (Levenson et al. 1998). Because this SNR is nearby and bright, it is an excellent target for studies of the interaction between a cloud and a blast wave (Fesen et al. 1992; Hester et al. 1994; Levenson & Graham 2001; Patnaude et al. 2002; Katsuda et al. 2016), grain destruction in shocks (Sankrit et al. 2010; Raymond et al. 2020c), and the evolution of cooling gas in radiative shocks (Raymond et al. 2020b, 2020c). The northern nonradiative shocks have been extensively studied (Raymond et al. 1980; Treffers 1981; Hester et al. 1994; Ghavamian et al. 2001; Salvesen et al. 2009; Medina et al. 2014; Katsuda et al. 2016). They present a relatively advantageous target because they are not associated with radiative shocks, and the preshock gas is fairly uniform. Particular studies have focused on electron–ion (Ghavamian et al. 2001; Medina et al. 2014) and ion–ion (Raymond et al. 2015) thermal equilibration, particle acceleration (Salvesen et al. 2009; Raymond et al. 2020c; Tutone et al. 2021), elemental abundances and charge-transfer emission (Nemes et al. 2008; Katsuda et al. 2011), and dust destruction (Raymond et al. 2013; Sankrit et al. 2014).

Here, we investigate the nonradiative shocks to the east of the bright radiative shocks. We use the Hectochelle instrument on the MMT telescope to obtain high-resolution Hα profiles, and we use images in Hα from 1993 to 2020 to measure proper motions. The distance to the Cygnus Loop is tightly constrained, so the proper motions give the shock speeds. The shocks in the east are slower than those in the north. We investigate the electron–ion equilibration in these shocks, and we also investigate the relationship between the nonradiative shocks and the radiative ones that lie 1′ to 5′ inside them.

The paper is organized as follows. Section 2 describes the imaging and spectral observation. Section 3 describes the measurement of proper motions from the images and Hα line profile parameters from the spectra. In Section 4, we discuss the roles of various shock precursors, compare to other observations, and discuss the spatial structure of the eastern Cygnus Loop. Section 5 summarizes our results.

2. Observations

The overall perspective is shown in Figure 1, an image of the entire Cygnus Loop in [O III], Hα, and [S II]. The nonradiative shocks we discuss here are the Hα filaments seen as wispy, red structures to the east of the SNR near the top-left corner of the image.

2.1. Images

In order to obtain shock speeds, we combine proper-motion measurements with the accurately known distance of 725 ± 15 pc that Fesen et al. (2018, 2021) derived from the Gaia distance to several stars superposed on the Cygnus Loop. The proper motions were obtained from wide-field Hα mosaics. The first mosaic was obtained by R. Fesen with the 0.6 m Case Western Reserve Burrell–Schmidt Telescope at Kitt Peak National Observatory on 1993 August 14. It employed a 20 Å wide filter and exposure times of 1500 s. The instrument setup was similar to that described in Fesen et al. (1992).

The second Hα image was obtained by amateur astronomer M. Xie through the heavy light pollution of a backyard in Coppell, TX. He used a Takahashi FSQ-106EDX III telescope with a 30 Å wide filter. The mosaic was constructed from 336 exposures of 300 s obtained between 2020 June 6 and September 27. Images in the [O III] and [S II] lines were obtained during the same period. More details are given at https://www.astrobin.com/ft1kwb/.

Figure 1 shows a superposition of Hα, [O III], and [S II] images obtained by M. Xie to indicate the relationship between the nonradiative shocks discussed here and the brighter radiative shocks that are visible in [O III] and [S II] as well as Hα. The nonradiative shocks show up as wispy, deep red filaments outside the bright emission regions in the east, and they continue around the north to the northwest. The nonradiative shocks in the north encounter a fairly uniform medium whose density is around 0.2–0.5 cm^{-3} (Raymond et al. 2003; Fesen et al. 2021), while the radiative shocks appear where SNRs encounter densities of 2 to 10 cm^{-3} (Raymond et al. 2020b). There are two plausible interpretations of the morphology. In the east, it appears that the shock has encountered a fairly dense cloud (Hester et al. 1994), but the shock has progressed faster through lower-density gas surrounding the cloud, so the nonradiative filaments are seen in projection just ahead of the shocked cloud. Alternatively, it is possible that the Hα filaments show the current position of the shock front, but the highly ionized postshock gas is invisible in the optical until it cools and recombines an arcminute or so behind the shock. In any case, faint, diffuse Hα emission is apparent just outside of the eastern nonradiative filaments, and it arises from recombination and collisional excitation in the photoionized precursor (Levenson et al. 1998; Danforth et al. 2000). We will use it below to constrain the preshock density and the 3D structure.

We performed the astrometric calibration in two steps: (i) using the Astrometry.net web service[12] (Lang et al. 2010), we corrected large-scale offsets in the World Coordinate System (WCS) for the Burrell–Schmidt image and derived the WCS from scratch for M. Xie's image; (ii) then, we used the WCS returned by Astrometry.net as an initial guess for the routine for MMIRS infrared images (Grishin & Chilingarian 2021) that derives both the celestial and distortion components of the coordinate system. In this procedure, the catalog of point-like sources delivered by the SExtractor (Bertin & Arnouts 1996) is cross-matched against the PanSTARRS-DR2 catalog with a maximum coordinate error of 3″. To resample both images onto the same WCS, we used the astropy-affiliated reproject package[13] (Astropy Collaboration et al. 2013, 2022). To prevent systematics caused by interpolations when reprojecting an image in an undersampled mode, we used Burrell–Schmidt images with a better resolution as a reference.

[12] https://astrometry.net/
[13] https://reproject.readthedocs.io/en/stable/

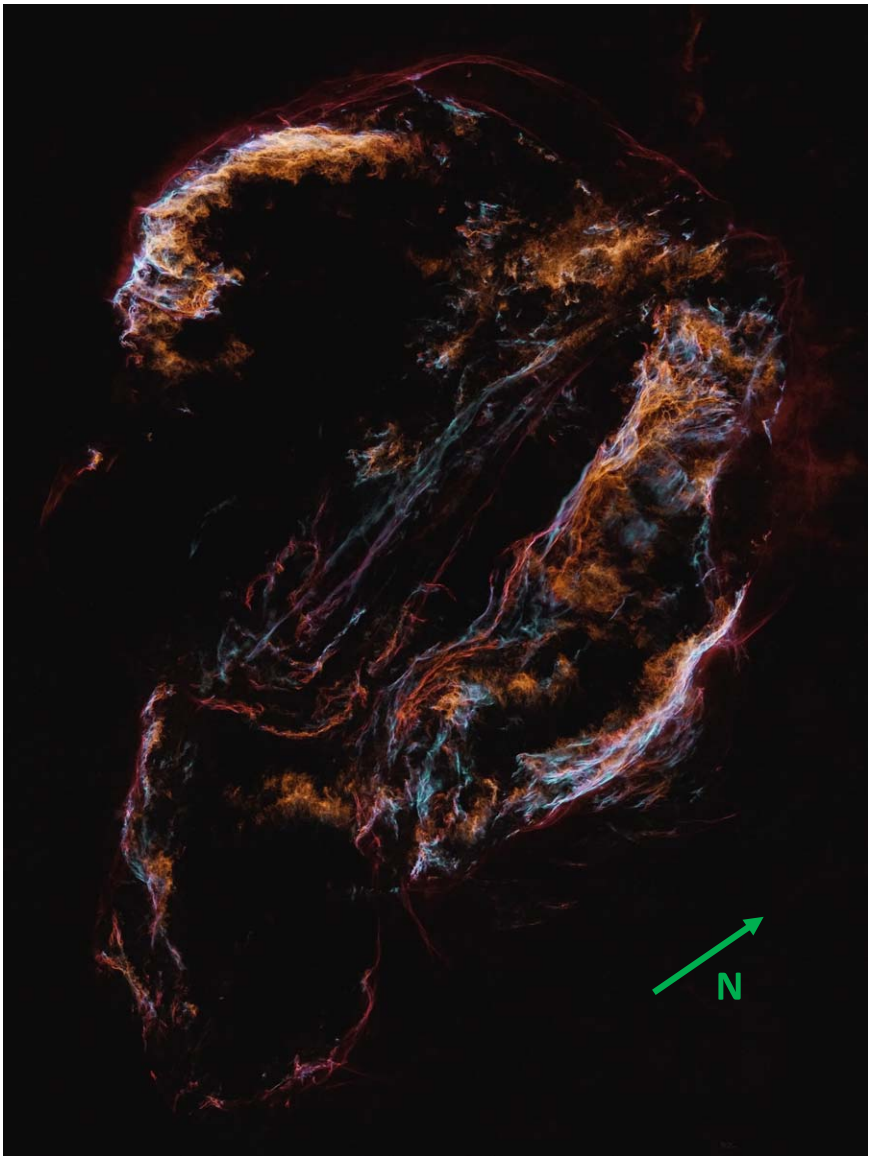

Figure 1. Image of the Cygnus Loop in [O III] (blue), Hα (red), and [S II] (green), produced by Min Xie. Stars have been removed using StarNet++. The Cygnus Loop is about 2° by 3°, and north is indicated by the green arrow. The nonradiative shocks are visible as the wispy red filaments around the northern part of the SNR. The northern region was studied by Salvesen et al. (2009) and Medina et al. (2014). Here, we study the eastern filaments.

2.2. Hectochelle Observations

The Hectochelle is a multiobject echelle spectrograph on the MMT telescope located at Mt. Hopkins, Arizona (Szentgyorgyi et al. 2011). Its 240 optical fibers are 1.″5 in diameter, and they can be placed over a 1° field subject to constraints that the distance between fibers be at least 25″ and that the fibers do not cross each other. We selected positions mostly based on low-resolution spectra from LAMOST that showed emission lines associated with the Cygnus Loop (Seok et al. 2020), but some positions were added specifically to cover the Balmer line filaments at the eastern edge of the Cygnus Loop. Observations were obtained during 2020 and 2021 covering the Hα and [N II] lines near 6560 Å and the [O III] lines at $\lambda\lambda$5007, 4959. Over 200 of the positions pertain to radiative shocks; we will analyze them in a separate paper. Here, we analyze the spectra that showed pure Balmer line emission from nonradiative shock waves. A few other positions showed pure Balmer spectra, but the signal-to-noise ratio was poor due to the faintness of the emission or contamination by a star. The spectra were obtained with the OB 25 filter, which covered the range of 6465–6645 Å, and the spectral resolution was about 36,000, as judged from the night-sky lines.

Hα observations of the eastern region were obtained on the nights of 2021 October 28 and 2021 November 27. The exposure times on the two nights were 5640 and 4800 s, and the airmasses were 1.774 and 1.283. The 10 positions studied here are given in Table 1, and they are shown on the 2020 Hα image in Figures 2–5. Note that spectra 084 on October 28 and 104 on November 27 are the same position, but they were observed with different optical fibers. They were analyzed separately to check the consistency of the spectral fits.

The flux calibration was based on Gaia stars included in the fiber configuration. An input Hectochelle spectrum of a star is fitted by a linear combination of stellar templates: either an empirical spectrum from the recalibrated UVES-POP stellar

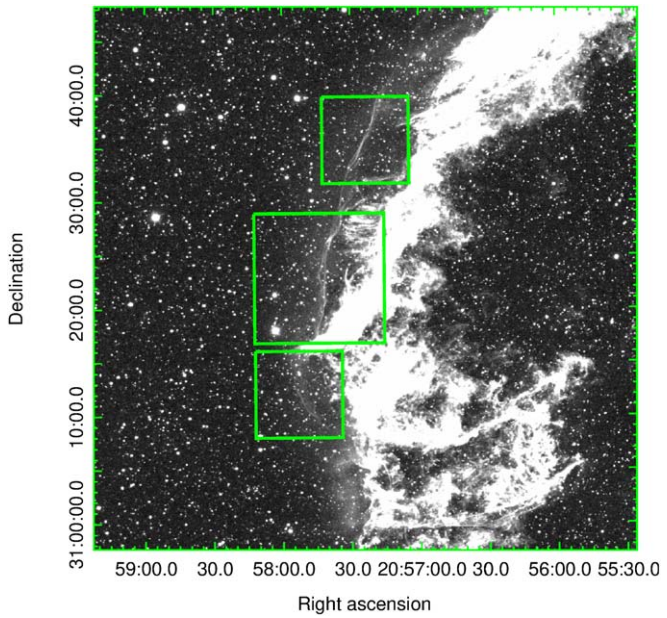

Figure 2. Eastern Cygnus Loop from the 2020 Hα image. Boxes indicate the regions of the subsequent figures that show the fiber positions.

Table 1
Hectochelle Fiber Positions

Pos	R.A. (J2000)	Decl. (J2000)
2021 October 28		
084*	20:57:20.678	31:37:28.63
117	20:57:44.065	31:22:51.13
124	20:57:42.801	31:19:19.33
136	20:57:53.795	31:12:15.09
2021 November 27		
101	20:57:28.327	31:33:40.53
104[a]	20:57:20.678	31:37:28.63
105	20:57:26.610	31:34:22.30
109	20:57:25.079	31:35:22.92
121	20:57:40.549	31:26:11.35
158	20:57:52.408	31:11:48.49

Note.
[a] Positions 084 on 2021 October 28 and 104 on November 27 are the same, but they were analyzed separately as a consistency check.

library (Borisov et al. 2023) or a PHOENIX (Husser et al. 2013) synthetic stellar atmosphere. Our fitting procedure uses a multiplicative polynomial continuum and also shifts and broadens the templates to account for radial velocity and stellar rotation. This code was originally developed as a telluric correction routine for our own MagE and FIRE data-reduction pipelines (Chilingarian 2020). Then, we use the weights of best-fitting templates from a linear combination determined by the fitting code to assemble the best-fitting template in the entire optical domain (including the areas outside the fitting region), which is then integrated with the Gaia *G* filter throughput curve to determine flux normalization. Then, a stellar spectrum from Hectochelle is matched against this renormalized template and a flux conversion vector is computed as their ratio. This approach gives results consistent within 7% wavelength-dependent variations.

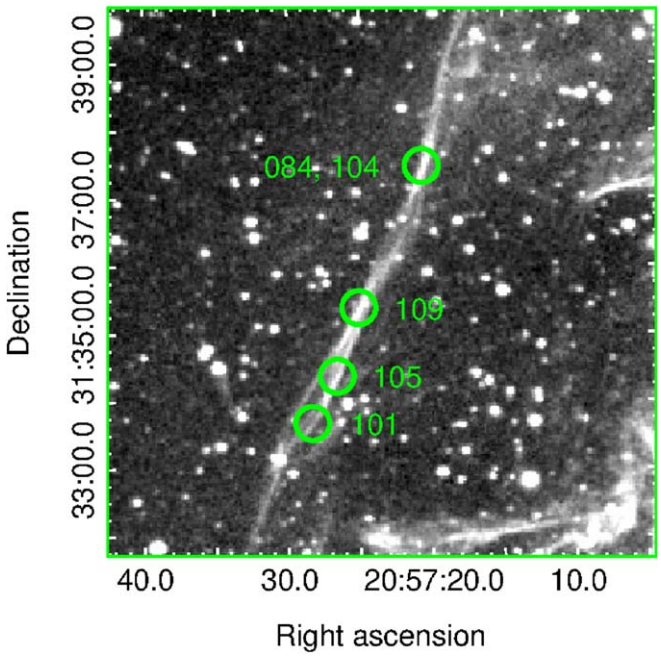

Figure 3. Positions of the four northern fibers superposed on the Hα image obtained in 2020. Spectra 084 and 104 were obtained at the same position on 2021 October 28 and 2021 November 27, respectively. Circles are 15″ in radius for clarity. The actual fiber diameter is 1.″5.

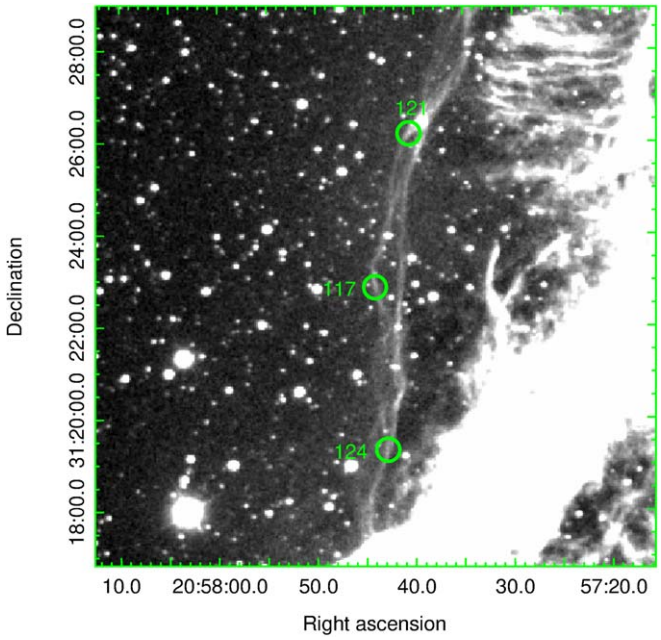

Figure 4. Positions of the three central fibers superposed on the Hα image obtained in 2020. Circles are 15″ in radius for clarity. The actual fiber diameter is 1.″5.

We validated our approach against direct flux calibration using Gaia blue photometer (BP)/red photometer (RP) low-resolution spectra in the [O III] setup obtained on 2020.0930, where bright stars (10–12.5 mag) were included into the configuration, and several of them had Gaia BP/RP spectra. However, we note that the 1.″5 fiber diameter means that some of the stellar flux might be lost, and the stellar calibration yields a sensitivity about 30% lower than shown in Szentgyorgyi et al. (2011). It is therefore possible that the derived fluxes of diffuse nebular emission are overestimated by as much as 30%.

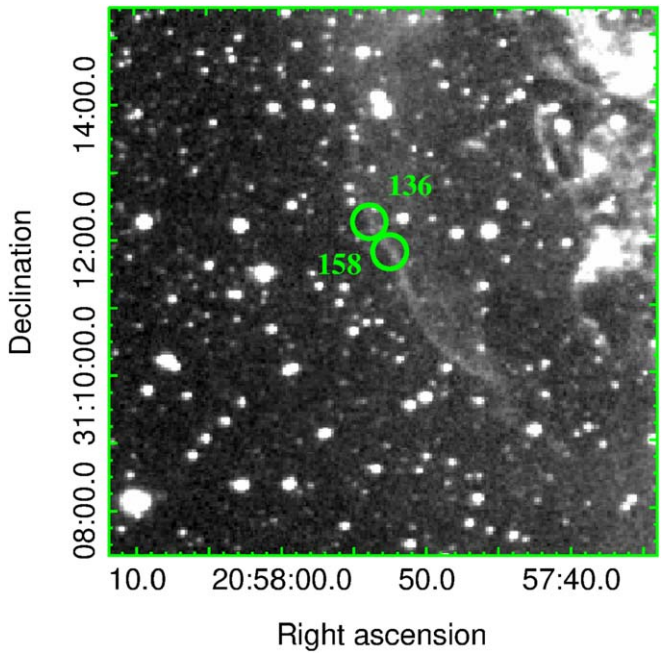

Figure 5. Positions of the four northern fibers superposed on the Hα image obtained in 2020. Circles are 15″ in radius for clarity. The actual fiber diameter is 1.″5.

3. Analysis

3.1. Images

We measured proper motions by resampling the data to 0.″208 pixels, selecting a region around each fiber position, and performing 2D cross-correlations between the 1993 and 2020 images in Fourier space using the modified IDL function MPFIT2DPEAK (Markwardt 2009). The modification allowed us to fit a tilted 2D Gaussian profile plus an empirical additive component. We did this to account for a complex two-component shape of the correlation function: a central narrow component coming from field stars with very little proper motion, and an offset tilted component strongly extended in one direction related to narrow sharp filaments in the nebula. The central component is calculated first by computing a 2D cross-correlation function of a single bright star located relatively close to the position of the nonradiative shock but in a narrow window that does not include any filaments. This is done using the original version of MPFIT2DPEAK. Under an ideal situation, this reference correlation function will be a circular Gaussian centered at (0, 0). However, because of the noncircular point-spread functions of both images, which also vary across the field of views, it has a more complex shape and sometimes might be slightly offset from the center. Then, we supply the stellar 3D cross-correlation function as an additive component to the the modified minimization routine, and determine parameters of an elongated shifted 2D Gaussian, which corresponds to the proper motion of the nonradiative shock. We note that the uncertainties for some positions are quite large, while that for position 121 is unrealistically small. The proper motions are converted to shock speeds assuming that the distance to the Cygnus Loop is 725 pc (Fesen et al. 2021). Results are given in Table 4.

3.2. Line Profiles

The sky-subtracted Hectochelle Hα profiles were fit with the sum of two Gaussians plus a linear background using the mpfit package in IDL (Markwardt 2009). The [N II] lines were measured separately. Figures 6 and 7 show the fits, and Table 2 gives the fit parameters for the 10 positions along the Balmer line filaments. As discussed in Section 2.2, the intensities may be overestimated by up to 30%, but the ratio of broad-to-narrow component intensities, I_B/I_N, does not depend on the calibration. The centroid velocities, $V_{\rm LSR}$, are given in the local standard of rest, and the narrow- and broad-component line widths (FWHM) are given in kilometers per second.

We have a consistency check on the fitting procedure. Positions 084 on 2021 October 28 and 104 on 2021 November 27 are the same position on the sky observed with different optical fibers. We would expect that the values of I_B/I_N and [N II]/Hα might differ because differences in seeing could change the amount of narrow precursor emission falling onto the fiber. We might also expect some difference in the total intensities, since the throughputs of the optical fibers are known to vary by about 10%. We see from Table 2 that the differences in the values of I_B/I_N fall somewhat outside the 1σ errors, but that the other fit parameters agree to within the expected uncertainties. We note that [N II] emission is present at the level of a few percent of the Hα brightness. For reasonably complete electron–ion equilibration at the shock, as indicated below, the ratio of Hα-to-[N II] would be roughly the abundance ratio, or about 10^4 according to the excitation and ionization rates in CHIANTI (Del Zanna et al. 2015), so the [N II] must come from imperfectly subtracted background or from a shock precursor. The former would imply some inaccuracy in I_B/I_N. The latter is discussed below.

4. Discussion

4.1. Photoionization Precursor

Faint, diffuse Hα emission from a photoionization precursor was noted by Levenson et al. (1998) and Danforth et al. (2000). In the north, the time-dependent temperature and ionization state were modeled by Medina et al. (2014). The ionization was due primarily to He I and He II photons from the nonradiative shock, and the heating was strong because of their high photon energies. Those authors found that the ∼0.2 $\rm cm^{-3}$ gas was heated as it approached the shock, and that the [N II]/Hα ratio was of order 10%. In the east, we find a typical Hα surface brightness of 75 Rayleighs, based on star-free regions in the 1993 image just ahead of the fiber positions in the diffuse regions and in background regions farther upstream, using the Hα intensities in Table 2 to determine the flux scale of the image. Figure 8 shows the brightness in a 10″ wide band across the filament near our position 121 based on the 2020 Hα image with stars removed. The brightness rises from the constant background level starting at about 900″ up until the filaments are encountered at 1080″–1150″, followed by a slight drop from the preshock brightness.

The photoionization precursor can heat the gas enough to significantly affect the width of the narrow component. According to the models of Medina et al. (2014), the photoionized gas can be as hot as 17,000 K, which would give a 28 $\rm km\,s^{-1}$ wide narrow line width. That does not account for the 36 $\rm km\,s^{-1}$ widths measured here and by

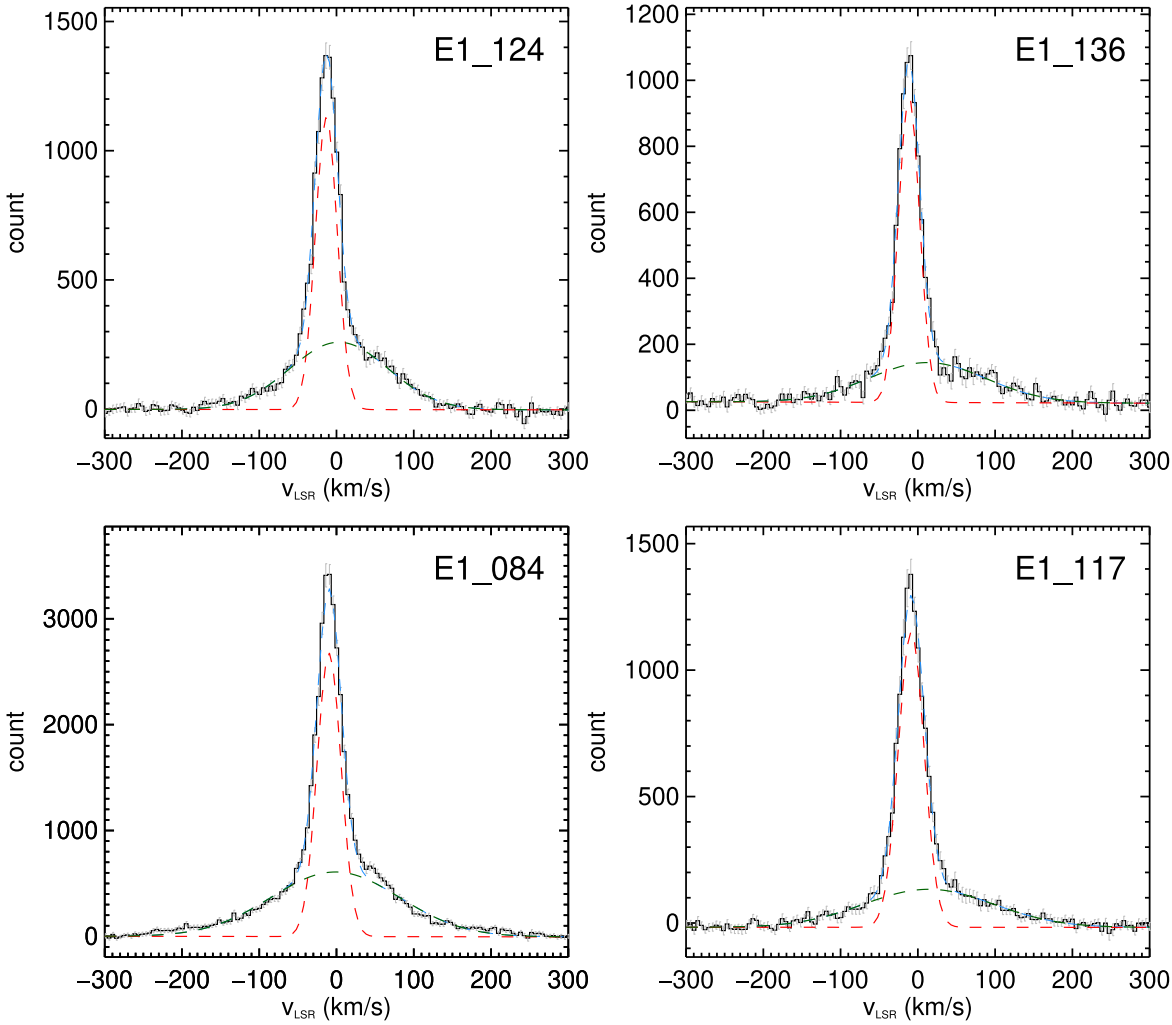

Figure 6. Hα profiles with Gaussian fits for the night of 2021 October 28. Narrow and broad components are shown as dashed lines, and the data are shown as the solid line.

Medina et al. (2014), so some additional turbulence or heating in a narrow precursor is required. The heating in the photoionization precursor has an interesting implication: If the gas is roughly half neutral and half ionized, the collisional excitation of neutrals dominates the Hα emission by perhaps an order of magnitude, as opposed to most photoionized nebulae where recombination dominates.

Two of the Hectochelle fibers produced good spectra of the precursor emission. Fiber 080 from October 28 at $20^h57^m13\overset{s}{.}3990$, $+31°41'\ 36\overset{''}{.}6430$ lies about 20″ ahead of the shock and about 4′ north of our northernmost position (084 on October 28 and 104 on November 27). Fiber 170 from 27 November lies at $20^h57^m40\overset{s}{.}0000$, $+31°01'\ 49\overset{''}{.}3960$. That is south of the regions we consider here, and it is in the diffuse emission near the bottom edge of Figure 2, about 3′ ahead of the shock. Both spectra show line widths of about 26 km s^{-1}, and the ratios of [N II] to Hα are 0.09 and 0.16, respectively. The line widths correspond to a temperature of 15,000 K, which is in line with the heating in the precursor predicted and observed by Medina et al. (2014). At that temperature, the collisonal excitation rate for Hα is 10 times the recombination rate to produce Hα, so that if the neutral fraction is 0.5, the precursor Hα emission is dominated by collisional excitation rather than recombination. The line width is similar to that measured by Katsuda et al. (2016) farther north, though the depth along the line of sight (LOS) is 5 to 10 times larger.

The excitation rate is quite sensitive to temperature, but we will assume $T = 15{,}000$ K and take the emissivity to be $1.2 \times 10^{-12}\, n_e\, n_{\rm H\,I}$ erg cm^{-3} s^{-1}. The radius of the Cygnus Loop is about 21 pc (Fesen et al. 2018). If the photoionization precursor is about 2′ thick (0.4 pc at 725 pc), the thickness along the LOS is about 8 pc according to the sagitta relation. With that LOS depth, an electron density of about 2.4 cm^{-3} gives the observed Hα intensity with the collisional excitation at the temperature given above (Callaway 1994), so if the preshock ionization fraction is 0.5, the total preshock density is 5 cm^{-3}. That is comparable to the preshock density of the radiative shocks entering the cloud to the west of the Cygnus Loop (Raymond et al. 2020b), which seems consistent in that the brightnesses of radiative shocks in the eastern and western clouds are similar.

The next question is whether the precursor is associated with the radiative shocks, the nonradiative shocks, or both. To answer that question, we consider the brightness profile across the nonradiative shocks. If the filaments are planar shocks seen edge-on, and if they occupy the entire portion of the LOS where the precursor emission is seen, then the brightness will drop sharply behind the shock because the neutrals are ionized

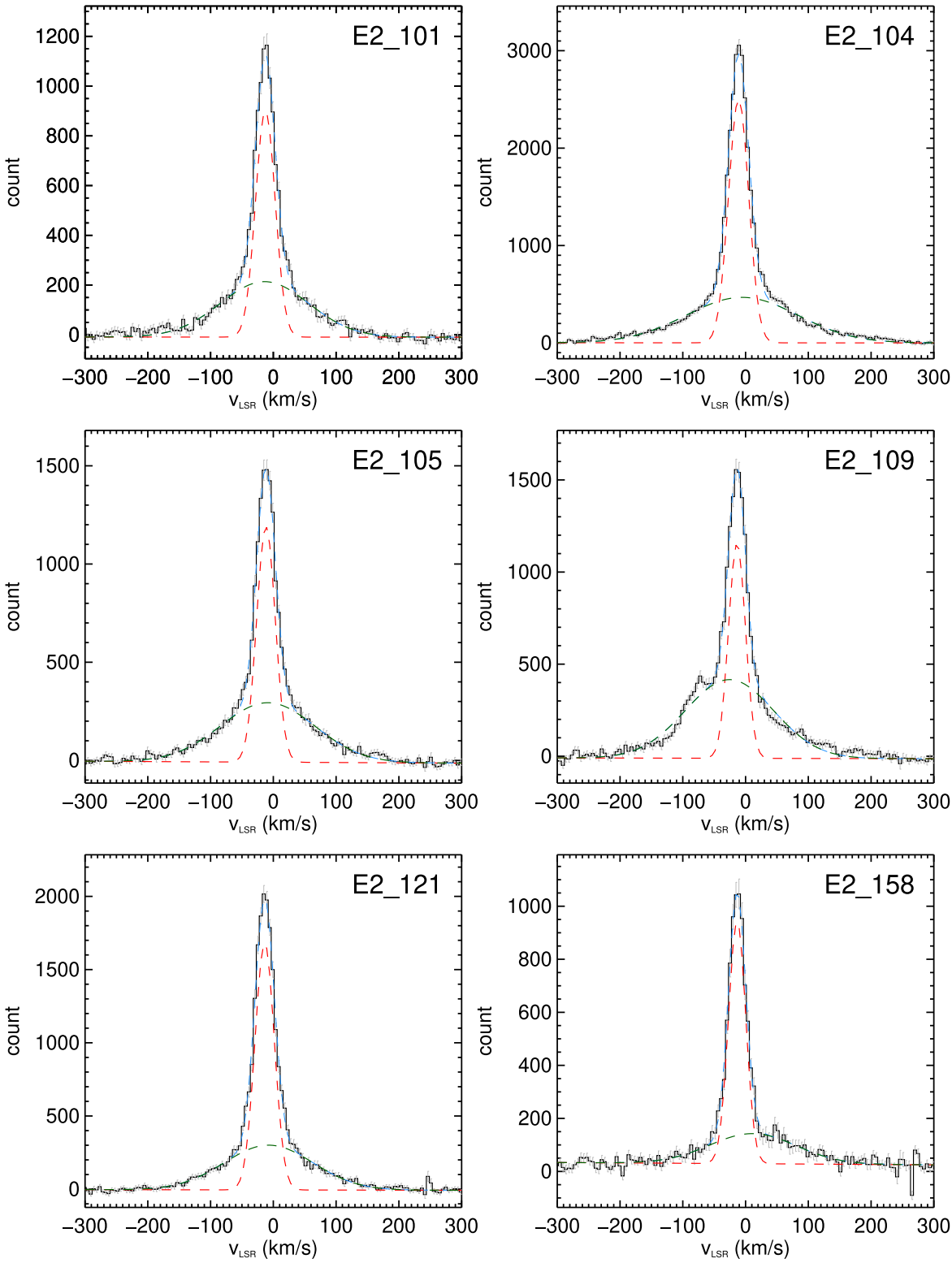

Figure 7. Hα profiles with Gaussian fits for the night of 2021 November 27.

away, and Hα emission due to recombination in the hot postshock gas is faint. The brightness profiles across the Balmer filaments in multiple positions show a uniform background level beyond 3′ ahead of the shock. The brightness then rises linearly up to the filament, and drops to typically 80%–90% of the preshock brightness in the region just behind the filament. Taken at face value, this would suggest that only 10%–20% of the precursor emission is associated with the nonradiative shocks. The actual shocks are curved, and it is likely that a somewhat larger fraction of the precursor comes from the nonradiative region. However, the overall picture seems most consistent with the idea that the nonradiative shocks are not physically ahead of the radiative shocks, but are seen in projection outside the radiative shocks. A simple

Table 2
Hα Intensities and Widths

Pos	I (Rayleighs)	I_B/I_N	VLSR$_N$ (km s^{-1})	FWHM$_N$ (km s^{-1})	VLSR$_B$ (km s^{-1})	FWMN$_B$ (km s^{-1})	[N II]/Hα_N
2021 October 28							
084	688	1.21 ± 0.03	-9.6 ± 0.3	36.7 ± 0.7	-1.4 ± 1.2	196 ± 3.2	0.02
117	218	0.65 ± 0.03	-8.6 ± 0.3	39.7 ± 0.7	14.1 ± 2.4	199 ± 6.4	0.06
124	242	1.03 ± 0.04	-13.1 ± 0.3	33.5 ± 0.7	3.3 ± 1.5	150 ± 3.7	0.16
136	189	0.72 ± 0.04	-11.4 ± 0.3	32.3 ± 0.8	12.6 ± 3.3	178 ± 8.1	0.07
2021 November 27							
101	225	1.11 ± 0.05	-12.7 ± 0.3	36.6 ± 0.9	-14.0 ± 1.6	166 ± 4.6	0.05
104	625	1.03 ± 0.02	-11.2 ± 0.2	37.9 ± 0.5	-5.4 ± 1.2	210 ± 3.3	0.02
105	304	1.28 ± 0.04	-11.7 ± 0.3	35.1 ± 0.7	-8.6 ± 1.3	177 ± 3.5	0.03
109*	344	1.91 ± 0.07	-13.6 ± 0.4	25.6 ± 1.3	-25.6 ± 1.3	166 ± 3.4	0.03
121	362	59 ± 11.2	0.13				
158	192	0.62 ± 0.04	-13.4 ± 0.4	32.3 ± 1.0	11.6 ± 4.2	163 ± 23	0.04

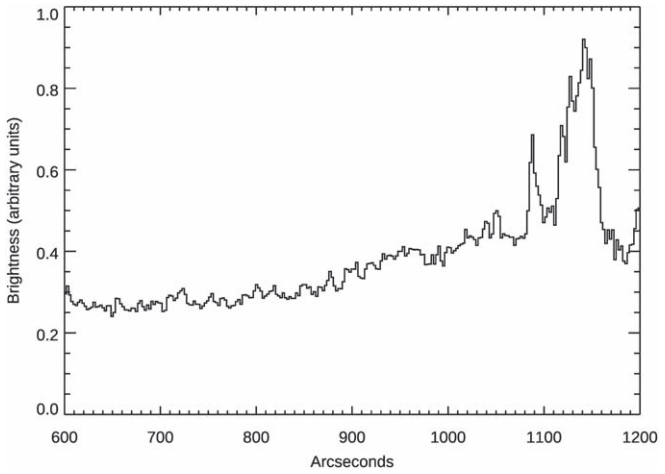

Figure 8. Hα brightness profile of the photoionization precursor and filament structure. The brightness units are arbitrary. The brightness increases gradually from the background value of about 0.25 to about 0.45 near the shock located at 1080″.

picture is that the blast wave has partially wrapped around the dense cloud in which radiative shocks produce bright emission.

An interesting side note is that Graham et al. (1991) report ridges of faint H_2 IR emission up to 2′ ahead of the bright optical filaments in the eastern Cygnus Loop, about 8′–10′ north of our northernmost fiber, and they may be associated with the Balmer filaments. The relative intensities of the 2.12 μm and other lines indicate an excitation temperature of 2200 K, and they show that the emission does not result from fluorescence or postshock molecule formation. The emission could in principle come from C-shocks, but the maximum speed of C-shocks is around 40 km s^{-1}, much lower than either the radiative or nonradiative shocks in this part of the Cygnus Loop. Photoionization heating by X-rays from the Cygnus Loop would produce broader H_2 precursors, because the mean free path for X-ray photons is large.

The H_2 ridges lie in a region where the diffuse Hα is about twice as bright as the precursor in the regions we have observed. Graham et al. (1991) attribute the H_2 emission to magnetic precursors driven by the nonradiative shocks and by shocks that are just becoming radiative, while fully radiative shocks produce enough UV emission to photodissociate the H_2. Such precursors require an Alfvén speed higher than the shock speed, which in turn requires an ionization fraction less than about 10^{-3} for the parameters assumed by Graham et al. (1991). However, the diffuse Hα emission requires an ionization fraction of order 0.5. We therefore consider it more likely that the H_2 ridges originate in molecular gas that is heated by the EUV emission of radiative and/or nonradiative shocks. By analogy with the heating of the photoionization precursors in atomic gas, each photoionization deposits considerable energy that can heat the gas until the heating is balanced by radiative cooling. The ionization lengths range from about $10''/n$ for photons close to the H I absorption edge to $100''/n$ for He II λ304 photons, so densities of order 10 cm^{-3} are needed to match the observed 20″ thicknesses of the H_2 ridges. Given the relatively high brightness of the Hα emission in those regions, that does not seem unreasonable. The question is whether the photoionization heating will produce a thick enough layer of 2000 K H_2 to match the observed fluxes. Models for time-dependent heating and dissociation of molecular gas by the hard EUV radiation from these shocks are needed to resolve that issue.

4.2. Cosmic Ray and Neutral Return Precursors

The photoionization precursor is quite thick, since it corresponds to the absorption lengths of the ionizing photons, especially He II λ304. A much thinner, but more intensely heated, precursor is produced by cosmic ray acceleration or by broad-component neutrals that overtake the shock and deposit their energy upstream (Hester et al. 1994). It can produce [N II] emission and Hα emission that contributes to the narrow component, because the plasma is heated and compressed. A strong constraint on the precursor thickness and electron heating is that the time spent in the precursor, given by the thickness L divided by the shock speed, times the ionization rate, $q_i(T)$, be small enough that neutrals survive to reach the shock, interact with postshock protons, and produce broad-component emission.

The Cygnus Loop nonradiative shocks must have such precursors, because the narrow-component FWHM values require heating and/or turbulence. In addition, excess [N II] is observed at one nonradiative shock (Fesen et al. 1982; Hester et al. 1986; Katsuda et al. 2016), indicating compression and heating of the plasma. The question remains whether the precursor is driven by cosmic rays or the flux of neutrals returning from downstream.

A cosmic ray precursor is required in the diffusive shock acceleration (DSA) model of particle acceleration, in which a

Table 3
Cygnus Loop Nonradiative Shock Observations

Paper	Region	N	FWHM$_B$	FWHM$_N$	I_B/I_N
Treffers (1981)	W	1	>130	35	0.5–5
Raymond et al. (1983)	NE	1	167	31	
Hester et al. (1994)	NE	6	130	32	
Ghavamian et al. (2001)	N	1	262		0.59
Medina et al. (2014)	N	12	245	37	0.87
Katsuda et al. (2016)	NE	1	130–230	29	0.75–2.01
This work	E	10	177	35	1.04

layer of upstream turbulence reflects particles back toward the shock (Blandford & Eichler 1987). The turbulence itself will broaden the line, and dissipation of the turbulence will heat the plasma (Boulares & Cox 1988), but it is hard to determine how much of the heat goes into electrons. The thickness of the precursor is given by $L = \kappa/V_s$, where κ is the cosmic ray diffusion coefficient. While the Cygnus Loop does produce nonthermal radio and gamma-ray emission, it is relatively faint. Both the radio and the gamma-ray emission of the radiative shock regions can be explained by simple adiabatic compression of the ambient cosmic ray electrons and protons, known as the van der Laan mechanism (van der Laan 1962; Raymond et al. 2020c). This would apply to perpendicular shocks, where the magnetic field is perpendicular to the shock motion, and in principle it does not require a turbulent precursor. For parallel shocks, reacceleration of the ambient cosmic rays (Uchiyama et al. 2010) is the preferred model. In any case, the energy that goes into accelerated particles is only about 2% of the energy dissipated by the shock (Tutone et al. 2021), so the cosmic ray precursor would be weak.

Precursors generated by neutrals returning across the shock should have a thickness given by the rate of ionization by charge transfer and electron collisions, and that is under 1″. A number of authors have investigated these precursors (Lim & Raga 1996; Raymond et al. 2011; Morlino et al. 2012; Ohira 2014), but none have dealt with the detailed plasma physics that would self-consistently determine how much energy is deposited upstream and how that energy is divided among turbulence, electron heating, and ion heating. Overall, however, the returning neutrals from fast shocks carry more kinetic energy, so they can provide more heat to the precursors of faster shocks.

4.3. Comparison to Other Measurements

Table 3 lists the measurements of Hα profiles of Balmer line filaments in different regions of the Cygnus Loop. For this work and the papers of Hester et al. (1994) and Medina et al. (2014), we list average values of the 6–12 positions observed. For Katsuda et al. (2016), we list the range measured at several positions where the slit crossed the complex filament. The range of broad-component widths in that filament complex is more than 100 km s^{-1}, which is not surprising given the wide range of positions observed and the fact that the region is on the verge of becoming a radiative shock (Raymond et al. 1983; Fesen & Itoh 1985; Hester et al. 1986; Long et al. 1992; Hester et al. 1994; Sankrit et al. 2000; Sankrit & Blair 2002). The narrow-component widths span a smaller range, but the values of I_B/I_N vary considerably, perhaps because of differing contributions of the photoionization and cosmic ray/return neutral precursors to the spectrum and the background spectrum.

It is notable that the spectra discussed in this work show broad-component widths only about three-quarters as large as those in the Medina et al. (2014) sample of positions along the northern boundary. The recently shocked cloud observed by Raymond et al. (1983), Hester et al. (1994), and Katsuda et al. (2016) shows somewhat smaller Hα widths, while the position in the north observed by Ghavamian et al. (2001) has a FWHM similar to those of Medina et al. (2014). The narrow-component widths are all similar, indicating that some heating or turbulence is needed beyond what a photoionization precursor could provide. Most of the observations give I_B/I_N smaller than we observe, and in fact smaller than the models of Ghavamian et al. (2001) predict. This might indicate that our background subtraction is more accurate, or that shock precursors are less important here than in the northern filaments. However, the scatter among the I_B/I_N values in our observations is substantial.

Another important comparison is the velocity centroid of the Hα narrow component to the velocity of the local H I cloud as determined from 21 cm emission, since the narrow component corresponds to the parameters of the preshock gas. The Hα centroids range from about –9 to –14 km s^{-1} (LSR), while the component of the H I 21 cm emission identified by Leahy (2003) as the northeastern cloud where the blast wave encounters denser material is centered at +4.8 km s^{-1} and suggests an expansion speed of 6 km s^{-1}. Katsuda et al. (2016) measured a narrow-component centroid of −5 km s^{-1} in the nonradiative shock in a small cloud somewhat to the north of our fields, and we find a centroid of −5.5 km s^{-1} in our two precursor spectra. The H I 21 cm emission seems to pertain to relatively dense gas, $n \sim 4$ cm^{-3}, which would correspond to the radiative shocks that are bright in [O III] and Hα, and perhaps to the photoionization precursor. Thus, it seems that the nonradiative shocks are produced by faster shocks in lower-density material either closer to the Sun or farther from it than the dense cloud, and that the lower-velocity material is moving at roughly 15 km s^{-1} relative to the dense gas in the cloud. This could be a more or less unrelated motion, or it could be a larger-scale aspect of the expansion reported by Leahy (2003), but which was not detected at 21 cm because of its low density.

The most extensive study of nonradiative shocks in the Cygnus Loop was the work of Medina et al. (2014), which also used Hectochelle. The principle difference between that paper and the present work is that the average broad-component width of the 12 spectra of Medina et al. (2014) was 244 km s^{-1}, while the average broad-component width of our 10 positions is 177 km s^{-1}. The average values of I_B/I_N for the Medina et al. (2014) sample and our sample are 0.87 and 1.04, respectively. Taken at face value, this indicates fairly complete thermal equilibrium (Ghavamian et al. 2001). However, the scatter among the I_B/I_N values at different positions is much larger than the measurement error, which suggests that background subtraction or a contribution from a shock precursor makes the values unreliable. The narrow-component line width in our sample is marginally smaller that that of Medina et al. (2014), averaging 34.6 km s^{-1} compared with 37.3 km s^{-1}. The surface brightnesses in our sample appear to be larger, which partly reflects a difference in calibration, though the Medina et al. (2014) sample includes some positions that are substantially fainter than the ones studied here.

Table 4
Electron–Ion Temperature Ratios from Proper Motions and FWHM

Position	Proper Motion ($''$ yr^{-1})	V_{PM} (km s^{-1})	V_{FWHM} (km s^{-1})	T_e/T_p
2021 October 28				
084	0.0877 ± .0077	308 ± 27	196 ± 3.2	1.08–1.35
117	0.0496 ± .0116	174 ± 41	199 ± 6.4	0.00–0.38
124	0.0611 ± 0.0088	215 ± 31	150 ± 3.7	0.75–1.30
136	0.0296 ± .0119	104 ± 42	178 ± 8.1	···
2021 November 27				
101	0.0688 ± .0149	242 ± 52	166 ± 4.6	0.56–1.40
104	0.0877 ± 0.0077	308 ± 27	210 ± 3.3	0.95–1.26
105	0.0856 ± .0281	301 ± 99	177 ± 3.5	0.55–1.64
109*	0.0886 ± .0063	311 ± 22	166 ± 3.4	1.38–1.53
121	0.0469 ± .0009	165 ± 3	167 ± 3.8	0.00–0.20
158	0.0568 ± .0139	200 ± 48	163 ± 23	0.00–1.18

If electrons and ions are fully equilibrated, the broad-component widths of Medina et al. (2014) imply an average shock speed for that sample of 338 km s^{-1}, while the average for our sample is 245 km s^{-1}, according to the relations between shock speed and line width of Ghavamian et al. (2001) and Morlino et al. (2013). If the electrons and ions did not equilibrate, the shock speeds would be 221 km s^{-1} and 161 km s^{-1}.

4.4. Electron–Ion Equilibration

There are three methods available to infer T_e/T_p from our observations. The first is to use the broad-component width and I_B/I_N, as was done by Ghavamian et al. (2001) and Ghavamian et al. (2013), for instance. Our average value of I_B/I_N shown in Table 3 and Figure 10 of Ghavamian et al. (2001) indicate fairly complete equilibration. The variation of the values of I_B/I_N among the 10 positions makes this somewhat suspect, but the models of Ghavamian et al. (2001) predict that I_B/I_N is about 3 for poorly equilibrated shocks in this range of shock speeds, and that it declines to about 1 for T_e/T_p larger than about 0.7.

The second method is to compare the shock speed determined from the proper motion with the proton temperature determined from the Hα broad component. Table 4 compares the proper-motion velocities (V_{PM}) with Hα line widths (V_{FWHM}). Assuming that He is fully ionized and the He ions and protons have the same temperatures, we use the Rankine–Hugoniot jump conditions and find that

$$T_e/T_p = 2.0 - (V_{FWHM}/(0.728\ V_{PM})^2. \quad (1)$$

Applying that to the upper and lower limits on V_{PM} in Table 4 leads to the ranges in T_e/T_p in the last column. The table shows that position 136 gives no solution, positions 117 and 121 indicate that $T_e/T_p \ll 1$, and the other six positions give T_e/T_p close to 1. The positions that give small values are the ones where the proper-motion shock speed is smallest. That might suggest a problem such as contamination of the filament emission by a stationary star, which would reduce the apparent motion in the cross-correlation, or that the shock is transitioning to the radiative phase and the nonradiative theory does not apply. Overall, we think that the observations are consistent with the Medina et al. (2014) result that T_e/T_p is close to 1, but we cannot draw a firm conclusion without better proper-motion measurements.

However, there is a third constraint. Temperatures from X-ray spectra are available for the northern filaments observed by Medina et al. (2014) in Salvesen et al. (2009), and they range from 1.7–2.2 × 10^6 K, similar to values obtained by Katsuda et al. (2011) and other investigations. That agrees with the full equilibration shock speed, but is more than twice what an unequilibrated shock would produce. We do not have temperatures from X-ray spectra in the east, but the ROSAT HRI images shown in Figure 8 of Levenson et al. (1999) and Figure 5 of Danforth et al. (2000) show that X-ray emission is present, though faint. Shocks slower than 200 km s^{-1}, as determined with the assumption of no equilibration, would yield electron temperatures below 0.05 keV even after Coulomb collisions brought T_e and T_p into equilibrium, and that is too cool to produce significant X-ray emission. The full equilibration shock speeds would give electron temperatures approaching 0.1 keV, producing detectable emission in the HRI band, which has significant effective area at photon energies around 0.3 keV. Slightly farther south, Danforth et al. (2000) observed UV emission from [Si VIII], which forms at log $T = 5.95$, and Szentgyorgyi et al. (2000) found a temperature of 1.1–1.2 × 10^6 K from the ROSAT PSPC X-ray spectrum. We have not been able to find a fit to the X-ray spectrum of the relevant region in the literature, but we note that a Chandra observation shown in the Supernova Remnant Catalog seems to show that the emission between the nonradiative and radiative filaments is fainter and cooler than that associated with the interaction between the blast wave and the cloud.[14]

Overall, our results are consistent with the observations of the faster shocks in the northern Cygnus Loop by Medina et al. (2014) that indicate fairly complete electron–ion equilibration ($T_e/T_p > 0.7$), but our observations do not provide tight constraints.

4.5. Overall Structure

An obvious feature of Figure 1 is that the Balmer line filaments we have observed lie roughly 2′ outside the bright [O III] emission of the eastern Veil Nebula, NGC 6992, and NCG 6995. The [O III], in turn, lies somewhat ahead of the bright Hα and [S II] emission. This structure can be interpreted in at least two ways. The first is that the Balmer filaments trace the position where a ∼200 km s^{-1} shock sweeps up neutral hydrogen atoms; the shock heats the gas of ∼600,000 K, and it gradually cools; as it cools, it gets denser, the cooling becomes more rapid, and when the temperature drops below 100,000 K the gas becomes bright in [O III]. The second is that the structure is merely a projection effect, in that the bright emission is produced by ∼100 km s^{-1} shocks in a relatively dense cloud that does not lie exactly at the limb. It might be displaced along the LOS from the SNR center, or it could be that a faster shock in lower-density gas has wrapped around the cloud.

The possibility that the bright optical filaments are plasma that passed through the nonradiative filaments and then cooled is appealing, because the combination of different observations would provide tight constraints on the shock properties. Something similar has been seen in slower shocks in lower-density gas in G70.0–21.5, where diffuse [O III] and Hα

[14] http://hea-www.cfa.harvard.edu/ChandraSNR/G074.0-08.5E/

emission follows sharp Hα filaments by about 20″ (Raymond et al. 2020a). The cooling distance behind a 240 km s^{-1} shock is about $10^{17}/n_0$ cm (Hartigan et al. 1987), or about $10''/n_0$ at the distance of the Cygnus Loop. While densities of order 0.1 cm^{-3} could account for the observed separation, they are smaller than the density inferred from the photoionization precursor. Another potential problem is that the cooling region behind a ∼250 km s^{-1} shock is violently thermally unstable (Chevalier & Imamura 1982; Innes et al. 1987; Innes 1992; Sutherland et al. 2003), and the [O III] filaments are not as badly shredded as might be expected in that case.

The alternative interpretation is just projection of different shocks onto the plane of the sky. This has the advantages that the density estimate from the photoionization precursor does not pertain to the nonradiative shocks and that the separation between the Balmer line filaments and the bright [O III] region has no particular physical meaning. It is therefore perfectly compatible with the observation that the separation between the Balmer filaments and the [O III] filaments decreases from about 3′ in the north to zero in the south, and in fact pure Balmer line filaments lie behind the [O III] emission in some places (Figure 2 of Szentgyorgyi et al. 2000). It is plausible that the dense cloud responsible for the ∼150 km s^{-1} shocks is well in front of the center of the Cygnus Loop in the north, for instance, but it is at the limb in the east near our positions 124 and 136. The distortion of the surface of the SNR is far less extreme than is required to explain the radiative shock filaments that extend southward from Pickering's triangle across the center of the Cygnus Loop.

5. Summary

Hα line profiles of Balmer line filaments in the eastern Cygnus Loop were obtained with Hectochelle. They show broad-component widths of 150–210 km s^{-1}, indicating shock speeds of 150–210 km s^{-1} if electrons and ions do not equilibrate, or 210–290 km s^{-1} if electrons and ions are fully equilibrated. Comparison of the shock speeds derived from proper motions with the Hα line widths suggest inefficient equilibration in two slow shocks, but six of the positions indicate efficient equilibration. The intensity ratios of the broad and narrow components and the observed X-ray emission also indicate $T_e/T_p \geqslant 0.7$. The shocks in the eastern Cygnus Loop are somewhat slower than those in the northern Cygnus Loop studied by Medina et al. (2014), and they support the conclusion that relatively slow, collisionless shocks efficiently equilibrate electrons and protons (Raymond et al. 2023).

The widths of the narrow components are 32–38 km s^{-1}, in keeping with the values measured in somewhat faster shocks in the northern Cygnus Loop by Medina et al. (2014). They are larger than the line widths in the photoionization precursor, where the 15,000 K temperature estimated from the line width agrees with that predicted theoretically by Medina et al. (2014). For a gas that is roughly half ionized, that would imply that collisional excitation rather than recombination dominates the Hα emission in the photoionized gas. A narrow precursor created by cosmic rays or by a returning flux of broad-component neutrals is needed to further increase the narrow-component width to the values observed in the filaments.

We find that the densities ahead of the Balmer line filaments are on the order of 5 cm^{-3}, but the uncertainties are substantial and this density probably pertains to the photoionization precursor associated with the radiative shocks. However, this density is in line with other estimates of the densities in the eastern Cygnus Loop.

Further UV or X-ray studies of the eastern Cygnus Loop and improved proper motions from higher-resolution images would tighten the constraints on electron–ion equilibration, precursor properties, and the geometrical structure. In addition, we plan to analyze the Hectochelle line profiles of [O III] and Hα to determine the ram pressures and other properties of radiative shocks in the eastern and central Cygnus Loop.

Acknowledgments

We thank the staff of the MMT for carrying out these observations. B.C.K. was supported by the Basic Science Research Program through the National Research Foundation of Korea (NRF) funded by the Ministry of Science, ICT and Future Planning (grant No. 2020R1A2B5B01001994). This work was supported by the K-GMT Science Program (PID: MMT-2020B-003, MMT-2021B-003) of the Korea Astronomy and Space Science Institute (KASI).

Facility: MMT(HECTOCHELLE).

Software: SWarp (Bertin et al. 2002), mpfit (Markwardt 2009).

ORCID iDs

John C. Raymond https://orcid.org/0000-0002-7868-1622
Ji Yeon Seok https://orcid.org/0000-0002-0070-3246
Bon-Chul Koo https://orcid.org/0000-0002-2755-1879
Igor V. Chilingarian https://orcid.org/0000-0002-7924-3253
Kirill Grishin https://orcid.org/0000-0003-3255-7340
Nelson Caldwell https://orcid.org/0000-0003-2352-3202
Robert Fesen https://orcid.org/0000-0003-3829-2056

References

Astropy Collaboration, Price-Whelan, A. M., Lim, P. L., et al. 2022, ApJ, 935, 167
Astropy Collaboration, Robitaille, T. P., Tollerud, E. J., et al. 2013, A&A, 558, A33
Bertin, E., & Arnouts, S. 1996, A&AS, 117, 393
Bertin, E., Mellier, Y., Radovich, M., et al. 2002, in ASP Conf. Ser. 281, Astronomical Data Analysis Software and Systems XI, ed. D. A. Bohlender, d. Durand, & T. H. Handley (San Francisco, CA: ASP), 228
Blandford, R., & Eichler, D. 1987, PhR, 154, 1
Borisov, S. B., Chilingarian, I. V., Rubtsov, E. V., et al. 2023, ApJS, 266, 11
Boulares, A., & Cox, D. P. 1988, ApJ, 333, 198
Bychkov, K. V., & Lebedev, V. S. 1979, A&A, 80, 167
Callaway, J. 1994, ADNDT, 57, 9
Chevalier, R. A., & Imamura, J. N. 1982, ApJ, 261, 543
Chevalier, R. A., & Raymond, J. C. 1978, ApJL, 225, L27
Chilingarian, I. 2020, in ASP Conf. Ser. 522, Astronomical Data Analysis Software and Systems XXVII, ed. P. Ballester et al. (San Francisco, CA: ASP), 623
Danforth, C. W., Cornett, R. H., Levenson, N. A., Blair, W. P., & Stecher, T. P. 2000, AJ, 119, 2319
Del Zanna, G., Dere, K. P., Young, P. R., Landi, E., & Mason, H. E. 2015, A&A, 582, A56
Fang, J., Yu, H., & Zhang, L. 2017, MNRAS, 464, 940
Fesen, R. A., Blair, W. P., & Kirshner, R. P. 1982, ApJ, 262, 171
Fesen, R. A., & Itoh, H. 1985, ApJ, 295, 43
Fesen, R. A., Kwitter, K. B., & Downes, R. A. 1992, AJ, 104, 719
Fesen, R. A., Weil, K. E., Cisneros, I., Blair, W. P., & Raymond, J. C. 2021, MNRAS, 507, 244
Fesen, R. A., Weil, K. E., Cisneros, I. A., Blair, W. P., & Raymond, J. C. 2018, MNRAS, 481, 1786
Ghavamian, P., Raymond, J., Smith, R. C., & Hartigan, P. 2001, ApJ, 547, 995
Ghavamian, P., Schwartz, S. J., Mitchell, J., Masters, A., & Laming, J. M. 2013, SSRv, 178, 633

Graham, J. R., Wright, G. S., Hester, J. J., & Longmore, A. J. 1991, AJ, 101, 175
Grishin, K., & Chilingarian, I. 2021, arXiv:2112.01620
Hartigan, P., Raymond, J., & Hartmann, L. 1987, ApJ, 316, 323
Heng, K. 2010, PASA, 27, 23
Hester, J. J., Raymond, J. C., & Blair, W. P. 1994, ApJ, 420, 721
Hester, J. J., Raymond, J. C., & Danielson, G. E. 1986, ApJL, 303, L17
Husser, T. O., Wende-von Berg, S., Dreizler, S., et al. 2013, A&A, 553, A6
Innes, D. E. 1992, A&A, 256, 660
Innes, D. E., Giddings, J. R., & Falle, S. A. E. G. 1987, MNRAS, 226, 67
Katsuda, S., Maeda, K., Ohira, Y., et al. 2016, ApJL, 819, L32
Katsuda, S., Tsunemi, H., Mori, K., et al. 2011, ApJ, 730, 24
Korreck, K. E., Raymond, J. C., Zurbuchen, T. H., & Ghavamian, P. 2004, ApJ, 615, 280
Laming, J. M., Raymond, J. C., McLaughlin, B. M., & Blair, W. P. 1996, ApJ, 472, 267
Lang, D., Hogg, D. W., Mierle, K., Blanton, M., & Roweis, S. 2010, AJ, 139, 1782
Leahy, D. A. 2003, ApJ, 586, 224
Levenson, N. A., & Graham, J. R. 2001, ApJ, 559, 948
Levenson, N. A., Graham, J. R., Keller, L. D., & Richter, M. J. 1998, ApJS, 118, 541
Levenson, N. A., Graham, J. R., & Snowden, S. L. 1999, ApJ, 526, 874
Lim, A. J., & Raga, A. C. 1996, MNRAS, 280, 103
Long, K. S., Blair, W. P., Vancura, O., et al. 1992, ApJ, 400, 214
Markwardt, C. B. 2009, in ASP Conf. Ser. 411, Astronomical Data Analysis Software and Systems XVIII, ed. D. A. Bohlender, D. Durand, & P. Dowler (San Francisco, CA: ASP), 251
Medina, A. A., Raymond, J. C., Edgar, R. J., et al. 2014, ApJ, 791, 30
Meyer, D. M. A., Langer, N., Mackey, J., Velázquez, P. F., & Gusdorf, A. 2015, MNRAS, 450, 3080
Morlino, G., Bandiera, R., Blasi, P., & Amato, E. 2012, ApJ, 760, 137
Morlino, G., Blasi, P., Bandiera, R., Amato, E., & Caprioli, D. 2013, ApJ, 768, 148
Nemes, N., Tsunemi, H., & Miyata, E. 2008, ApJ, 675, 1293
Ohira, Y. 2014, MNRAS, 440, 514
Patnaude, D. J., Fesen, R. A., Raymond, J. C., et al. 2002, AJ, 124, 2118
Raymond, J. C., Blair, W. P., Fesen, R. A., & Gull, T. R. 1983, ApJ, 275, 636
Raymond, J. C., Caldwell, N., Fesen, R. A., et al. 2020a, ApJ, 888, 90
Raymond, J. C., Chilingarian, I. V., Blair, W. P., et al. 2020b, ApJ, 894, 108
Raymond, J. C., Davis, M., Gull, T. R., & Parker, R. A. R. 1980, ApJL, 238, L21
Raymond, J. C., Edgar, R. J., Ghavamian, P., & Blair, W. P. 2015, ApJ, 805, 152
Raymond, J. C., Ghavamian, P., Bohdan, A., et al. 2023, ApJ, 949, 50
Raymond, J. C., Ghavamian, P., Sankrit, R., Blair, W. P., & Curiel, S. 2003, ApJ, 584, 770
Raymond, J. C., Ghavamian, P., Williams, B. J., et al. 2013, ApJ, 778, 161
Raymond, J. C., Slavin, J. D., Blair, W. P., et al. 2020c, ApJ, 903, 2
Raymond, J. C., Vink, J., Helder, E. A., & de Laat, A. 2011, ApJL, 731, L14
Raymond, J. C., Winkler, P. F., Blair, W. P., & Laming, J. M. 2017, ApJ, 851, 12
Salvesen, G., Raymond, J. C., & Edgar, R. J. 2009, ApJ, 702, 327
Sankrit, R., & Blair, W. P. 2002, ApJ, 565, 297
Sankrit, R., Blair, W. P., & Raymond, J. C. 2014, in IAU Symp. 296, Supernova Environmental Impacts, ed. A. Ray & R. A. McCray (Cambridge: Cambridge Univ. Press), 160
Sankrit, R., Blair, W. P., Raymond, J. C., & Long, K. S. 2000, AJ, 120, 1925
Sankrit, R., Williams, B. J., Borkowski, K. J., et al. 2010, ApJ, 712, 1092
Seok, J. Y., Koo, B.-C., Zhao, G., & Raymond, J. C. 2020, ApJ, 893, 79
Sutherland, R. S., Bicknell, G. V., & Dopita, M. A. 2003, ApJ, 591, 238
Szentgyorgyi, A., Furesz, G., Cheimets, P., et al. 2011, PASP, 123, 1188
Szentgyorgyi, A. H., Raymond, J. C., Hester, J. J., & Curiel, S. 2000, ApJ, 529, 279
Treffers, R. R. 1981, ApJ, 250, 213
Tutone, A., Ballet, J., Acero, F., D'Aì, A., & Cusumano, G. 2021, A&A, 656, A139
Uchiyama, Y., Blandford, R. D., Funk, S., Tajima, H., & Tanaka, T. 2010, ApJL, 723, L122
van der Laan, H. 1962, MNRAS, 124, 125
Zhou, X., Bocchino, F., Miceli, M., Orlando, S., & Chen, Y. 2010, MNRAS, 406, 223